

Probing surface defects of ZnO using formaldehyde

Cite as: J. Chem. Phys. **152**, 074714 (2020); <https://doi.org/10.1063/1.5138372>

Submitted: 14 November 2019 . Accepted: 20 January 2020 . Published Online: 20 February 2020

Yunjun Cao , Jie Luo, Wugen Huang, Yunjian Ling, Junfa Zhu , Wei-Xue Li , Fan Yang , and Xinhe Bao

COLLECTIONS

Paper published as part of the special topic on [Oxide Chemistry and Catalysis](#)

Note: This paper is part of the JCP Special Topic on Oxide Chemistry and Catalysis.



View Online



Export Citation



CrossMark

ARTICLES YOU MAY BE INTERESTED IN

[Molecular chemisorption of N₂ on IrO₂\(110\)](#)

The Journal of Chemical Physics **152**, 074712 (2020); <https://doi.org/10.1063/1.5142210>

[Atomic scale step structure and orientation of a curved surface ZnO single crystal](#)

The Journal of Chemical Physics **152**, 074705 (2020); <https://doi.org/10.1063/1.5138909>

[Reversible oxidation and reduction of gold-supported iron oxide islands at room temperature](#)

The Journal of Chemical Physics **152**, 074710 (2020); <https://doi.org/10.1063/1.5136279>

Lock-in Amplifiers
up to 600 MHz



Probing surface defects of ZnO using formaldehyde

Cite as: J. Chem. Phys. 152, 074714 (2020); doi: 10.1063/1.5138372

Submitted: 14 November 2019 • Accepted: 20 January 2020 •

Published Online: 20 February 2020



View Online



Export Citation



CrossMark

Yunjun Cao,¹  Jie Luo,² Wugen Huang,^{1,3} Yunjian Ling,^{1,3} Junfa Zhu,⁴  Wei-Xue Li,^{2,a)}  Fan Yang,^{1,a)} 
and Xinhe Bao¹

AFFILIATIONS

¹State Key Laboratory of Catalysis, Dalian Institute of Chemical Physics, Chinese Academy of Sciences, Dalian 116023, China

²School of Chemistry and Materials Science, Hefei National Laboratory for Physical Sciences at Microscales, University of Science and Technology of China, Hefei 230026, China

³University of Chinese Academy of Sciences, Beijing 100039, China

⁴National Synchrotron Radiation Laboratory, Collaborative Innovation Center of Suzhou Nano Science and Technology, University of Science and Technology of China, Hefei 230029, China

Note: This paper is part of the JCP Special Topic on Oxide Chemistry and Catalysis.

a) Authors to whom correspondence should be addressed: wxli70@ustc.edu.cn and fyang@dicp.ac.cn

ABSTRACT

The catalytic properties of metal oxides are often enabled by surface defects, and their characterization is thus vital to the understanding and application of metal oxide catalysts. Typically, surface defects for metal oxides show fingerprints in spectroscopic characterization. However, we found that synchrotron-radiation photoelectron spectroscopy (SRPES) is difficult to probe surface defects of ZnO. Meanwhile, CO as a probe molecule cannot be used properly to identify surface defect sites on ZnO in infrared (IR) spectroscopy. Instead, we found that formaldehyde could serve as a probe molecule, which is sensitive to surface defect sites and could titrate surface oxygen vacancies on ZnO, as evidenced in both SRPES and IR characterization. Density functional theory calculations revealed that formaldehyde dissociates to form formate species on the stoichiometric ZnO(10 $\bar{1}$ 0) surface, while it dissociates to formyl species on Vo sites of the reduced ZnO(10 $\bar{1}$ 0) surface instead. Furthermore, the mechanism of formaldehyde dehydrogenation on ZnO surfaces was also elucidated, while the generated hydrogen atoms are found to be stored in ZnO bulk from 423 K to 773 K, making ZnO an interesting (de)hydrogenation catalyst.

Published under license by AIP Publishing. <https://doi.org/10.1063/1.5138372>

I. INTRODUCTION

Metal oxide nanoparticles (NPs) expose a variety of surface defect sites, such as oxygen vacancies, steps, and kinks, which enable the catalytic functions of these NPs.^{1–3} As the catalytic properties of metal oxide NPs are increasingly exploited for a wide range of reactions, the design and improvement of oxide catalysts have been hampered by our limited understanding of the catalytic chemistry of oxide NPs.^{1–4} To elucidate the catalytic mechanisms over oxide catalysts, it is essential to characterize the structures and adsorption properties of their surface defects, which is much more challenging than probing surface sites of metal catalysts owing to the complexity and heterogeneity of oxide surfaces. To this end, a number of surface-sensitive techniques have been employed to study oxide NPs. For instance, photoelectron spectroscopy has been regularly

used to study the chemical and electronic states of oxides and to identify the electronic structures induced by surface reduction.^{5,6} Fourier-transform infrared (FT-IR) spectroscopy is another widely used technique for studying the chemical properties of oxide NPs. A probe molecule, such as CO, has typically been used to pinpoint the active sites of metals or to identify the adsorption and electronic properties of oxide surfaces.^{7,8} Over the past few decades, the above two techniques have been found to be effective in probing the surface defect sites of early transition metal oxides and rare earth metal oxides.^{4,5,7–10}

In comparison, the surface chemistry of metal oxides with a fixed valence state of cations has been even less understood despite their wide applications in catalysis.¹¹ For example, ZnO is a key catalytic material used in many industrial reactions, such as methanol synthesis,^{12–14} syngas conversion,¹⁵ and the water–gas

shift reaction.^{16,17} However, the chemical nature of the active sites on ZnO has not been understood despite the extensive studies on surface science and catalysis.^{12,13,15} Often, surface oxygen vacancies have been assumed as the active sites on ZnO for catalytic reactions. However, the lack of characterization techniques and probe molecules to identify such surface defects has made our understanding on the surface chemistry of ZnO elusive, which has remained as a subject of wide research interest in energy and catalysis.^{12–14}

In this study, we employed scanning tunneling microscopy (STM), X-ray photoelectron spectroscopy (XPS), synchrotron-radiation photoelectron spectroscopy (SRPES), and FT-IR spectroscopy to study ZnO(10 $\bar{1}$ 0) and ZnO powder catalysts. We found, while surface defects of ZnO are insensitive to SRPES or FT-IR spectroscopy using CO as a probe molecule, that formaldehyde could serve as an excellent probe molecule to detect and titrate surface oxygen vacancies of ZnO in FT-IR spectroscopy and SRPES. Density functional theory (DFT) calculations reveal that formaldehyde dissociates on the ZnO surface to form formate and formyl on the stoichiometric surface and the reduced surface, respectively. Accordingly, the dehydrogenation mechanism of formaldehyde on ZnO surfaces was also elucidated, where hydrogen atoms are found to be stored in the bulk of ZnO, making ZnO an interesting (de)hydrogenation catalyst. Since ZnO nanomaterials were often used as sensors for CH₂O or catalysts for CH₂O degradation,^{18–20} our study provides a mechanistic understanding of CH₂O adsorption and decomposition on ZnO surfaces, which is also the key to improve the performances of ZnO for the above applications.

II. EXPERIMENTAL AND COMPUTATIONAL METHODS

A. Model catalyst preparation and characterization

X-ray photoelectron spectroscopy (XPS) and synchrotron-radiation photoelectron spectroscopy (SRPES) were performed at the BL11U beamline in National Synchrotron Radiation Laboratory (NSRL), China. The end station of the BL11U beamline is a combined ultra-high vacuum (UHV) system including the analysis chamber, the preparation chamber, and a radial distribution chamber. The base pressures are 7×10^{-11} mbar, 2×10^{-10} mbar, and 7×10^{-11} mbar, respectively. The analysis chamber is equipped with a VG Scienta R4000 analyzer, a monochromatic Al K α X-ray source, a UV light source, low energy electron diffraction (LEED), and a flood electron gun. The clean ZnO(10 $\bar{1}$ 0) surfaces (8 mm \times 8 mm \times 1 mm, MTT) were prepared by cycles of 1 keV Ar⁺ ion sputtering and UHV annealing at 900 K. High purity metallic Zn (99.999%) was evaporated from a Al₂O₃ crucible onto ZnO(10 $\bar{1}$ 0) surfaces at 300 K. Here, the evaporation rate of Zn was calibrated on its growth on a Rh(111) surface. The BL11U beamline has an energy limit at 600 eV. Thus, for Zn LMM and Zn 2p spectra, we used a monochromatic Al K α X-ray source to measure. All XPS spectra were recorded at 300 K except for cryogenic adsorption experiments. STM experiments were performed in a custom-made Createc low-temperature STM system, with a base pressure below 4×10^{-11} mbar in the STM chamber. STM images were obtained at 78 K using an etched W tip and processed with the SPIP program from Image Metrology.

Powder ZnO and CeO₂ catalysts were prepared using the procedures described in previous studies.^{21,22} For FT-IR studies over ZnO powders, a high vacuum transmission infrared cell is employed,

with a base pressure of 5×10^{-9} mbar when the cryogenic manipulator was used. ZnO and CeO₂ powder samples were pressed separately on a tungsten mesh support, which was then connected to molybdenum rods for fast heating and cooling in the gas environment. A type K thermocouple is welded on the tungsten mesh, and the sample temperature can be controlled to ± 0.1 K accuracy between 120 K and 1000 K, via a combination of resistive heating and LN₂ cooling. The optical path inside the IR spectrometer was evacuated in order to avoid any unwanted IR adsorption from gas-phase species. IR spectra were recorded with 256 scans at 4 cm⁻¹ resolution.

B. Computational methods

Density functional theory (DFT)^{23,24} calculations were performed by the Vienna *ab initio* simulation package (VASP) using the projector augmented wave (PAW)^{25,26} potential and the generalized gradient approximation (GGA) in the form of the Perdew–Burke–Ernzerhof (PBE) exchange–correlation functional.²⁷ As shown previously,^{28–30} the method used (DFT, DFT+U) has little influence on the description of binding energy and reaction barriers. The plane wave basis set with a kinetic energy cutoff of 400 eV was used to solve the Kohn–Sham equations. ZnO(10 $\bar{1}$ 0) surfaces were modeled by a three double layer slab model with the (3 \times 2) periodicity separated by 12 Å vacuum along the Z-direction. The (2 \times 2 \times 1) k-point mesh was used to sample the Brillouin zone. The bottom-one layer of the slab was fixed until the residual forces of each atom were relaxed and the residual forces became less than 0.02 eV/Å. The climbing-image nudged elastic band (CI-NEB) method was used to identify the transition states. The STM images were simulated on the basis of Tersoff and Hamann’s formula^{31,32} using the bSKAN code.³³

III. RESULTS AND DISCUSSION

A. Structure and electronic structure of ZnO(10 $\bar{1}$ 0) surfaces

STM was first employed to characterize the surface structure of a UHV-prepared ZnO(10 $\bar{1}$ 0) surface, as shown in Fig. 1. In Fig. 1(a), the as-prepared ZnO(10 $\bar{1}$ 0) surface exhibits flat terraces by monatomic-height steps running along the two stable crystalline orientations, [0001] and [1 $\bar{2}$ 10]. Point defects could also be observed scarcely on the surface. On the flat terrace [Fig. 1(b)], bright lines with a 0.52 nm spacing along the [0001] direction were observed at positive bias voltages, which can be assigned to Zn atom rows since Zn 4s states occupy the conduction band minimum of ZnO.^{34,35} In Figs. 1(c) and 1(d), high-resolution STM images on the surface point defect show a dark spot at the bright Zn row with the expansion to adjacent dark rows. Figure 1(f) shows simulated STM images of oxygen vacancy and “Zn–O” dimer vacancy, respectively. From simulation, the “Zn–O” dimer vacancy shows the morphology similar to the dark spots observed in the STM image in accordance with the assignments in previous STM reports.^{34,36,37} Therefore, owing to the thermal stability of the ZnO(10 $\bar{1}$ 0) surface,^{37,38} except for steps and kink sites, surface defects observed on ZnO(10 $\bar{1}$ 0) prepared by UHV sputtering–annealing treatments are mainly, although very scarce, “Zn–O” dimer vacancy (<1%) on flat terraces, which can thus be regarded as the stoichiometric surface in the following discussion. Owing to its large bandgap, high formation energy of surface defects,

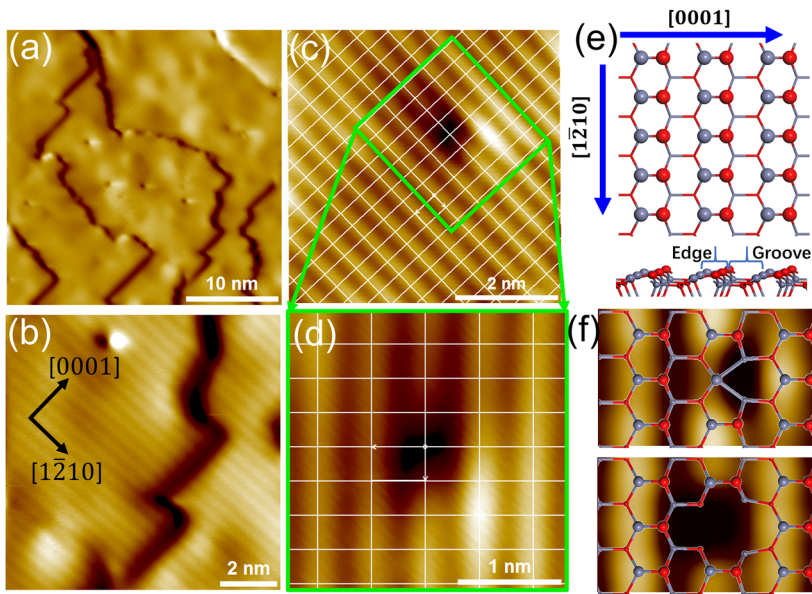


FIG. 1. [(a)–(d)] STM images of clean ZnO(10 $\bar{1}0$) surfaces. Scanning parameter: [(a) and (b)] $V_s = 2.5$ V, $I_t = 0.42$ nA and [(c) and (d)] $V_s = 2.9$ V, $I_t = 0.17$ nA. (e) Structural model of the ZnO(10 $\bar{1}0$) surface. Zn and O atoms are displayed in gray and red, respectively. (f) Simulated STM images of the ZnO(10 $\bar{1}0$) surface with an oxygen vacancy and “Zn-O” dimer vacancies, respectively.

and high temperature stability, a single crystal ZnO(10 $\bar{1}0$) surface could be hardly reduced under UHV conditions and exhibits mainly “Zn-O” dimer defects on terraces with standard UHV sputtering-annealing treatments.^{34,36,37} To simulate the reduced ZnO surfaces, which usually appeared in real catalysis, sub-monolayer metallic Zn was deposited onto the as-prepared ZnO(10 $\bar{1}0$) surface to form a highly defective Zn/ZnO(10 $\bar{1}0$) surface. The electronic structure of the Zn/ZnO(10 $\bar{1}0$) surface was characterized using XPS and SRPES, by recording corresponding O 1s, Zn LMM, Zn 2p, and valence band spectra. In Fig. 2, the as-prepared clean ZnO(10 $\bar{1}0$) surface exhibits an O 1s peak at 530.6 eV, Zn LMM peaks at 984 eV and 987.2 eV, Zn 2p peaks at 1021.6 eV and 1044.6 eV, and Zn 3d peak at ~ 10.5 eV, which are consistent with the standard XPS spectra of ZnO.^{39–41} After depositing 0.6 ML Zn atoms onto ZnO(10 $\bar{1}0$), no obvious features of metallic Zn could be observed in either Auger Zn LMM or Zn 2p spectra, while the intensity of the O 1s peak decreased by $\sim 10\%$, when compared to the O 1s spectra on the bare ZnO(10 $\bar{1}0$) surface. Thus, the deposited Zn atoms were oxidized by the oxygen on the ZnO surface, forming reduced ZnO nanoclusters with a decreased O/Zn atomic ratio. However, the defective ZnO surface cannot not be effectively distinguished from the bare ZnO(10 $\bar{1}0$) surface in XPS spectra, either in Auger Zn LMM, Zn 2p, or valence band spectra. After another deposition of 0.3 ML Zn atoms, the intensity of the O 1s peak was largely attenuated by $\sim 50\%$ with respect to the O 1s spectra on clean ZnO(10 $\bar{1}0$) surfaces. In this case, a new Auger peak of Zn LMM at 987.8 eV appears and the Zn 3d spectra evolve into a double-peak feature, both of which are typical characteristics on the formation of metallic Zn states,⁴⁰ indicating that the ZnO surface was starting to be covered by metallic Zn atoms. Note that, no obvious chemical shift can be observed in the Zn 2p spectra for Zn coverage ranging from 0.6 ML to 1.2 ML, which can be rationalized by the deep core level of Zn 2p, similar to the case of Cu 2p spectra with degenerate binding energies for Cu(0) and Cu(I) peaks.⁴² Therefore, highly sensitive SRPES can

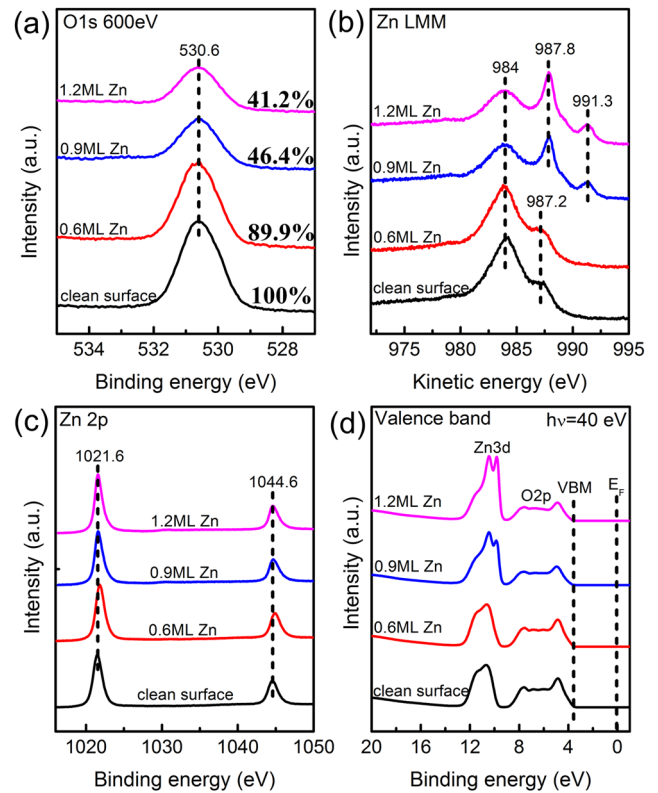


FIG. 2. O 1s, Zn LMM, Zn 2p, and valence band spectra of a single crystal ZnO(10 $\bar{1}0$) surface deposited with different coverage of metallic Zn. The photon energies of 600 eV and 40 eV were used for O 1s and valence band spectra, respectively. The Zn LMM and Zn 2p spectra are measured using an Al K-alpha X-ray source with a monochromator (1486.7 eV).

only be applied to differentiate the chemical states of metallic Zn and cationic Zn, but difficult in characterizing the subtle chemical environment change of ZnO surfaces with varying oxygen coordination numbers.

B. Formaldehyde as a probe to detect surface defects of ZnO

We then tried to use small molecules to probe surface defects of ZnO. The unsaturated local coordination environment could determine the adsorbate–surface interaction and the accompanying charge transfer, which could thus be monitored by both IR spectroscopy and SRPES. Compared to single crystal oxide surfaces,^{43–45} FT-IR spectroscopy is more extensively applied to oxide powders,¹⁰ the real form of technological oxide catalysts. Besides, the (10 $\bar{1}$ 0) surface is reported to be the dominantly exposed surface of ZnO powder after thermal treatment and accounts for more than 80% of their total area.^{38,46} Hereby, we chose also ZnO powders to perform adsorption experiments of probe molecules, by using a customized transmission FT-IR cell. The ZnO powder catalysts were prepared by the coprecipitation method, as described in detail previously.²¹ The stoichiometric ZnO sample we used is acquired by heating ZnO powder in 0.1 mbar O₂ at 673 K for 1 h (denoted as oxidized ZnO), while the highly reduced ZnO sample was prepared by annealing in 10 mbar CO at 673 K (denoted as reduced ZnO). Generally, for ZnO powder, reducing-atmosphere treatment is a facile strategy to generate oxygen vacancies,^{15,47} resulting in the reduction of ZnO in many reactions such as methanol synthesis, which can be hardly repeated on single crystal ZnO surfaces under UHV conditions.

As the most used molecule for probing surface active sites, CO was used first to probe surface defects of ZnO. Figure 3(a) shows that after exposing oxidized ZnO to the CO atmosphere at 120 K, a sharp peak at 2174 cm⁻¹ can be observed in IR spectra, which is in accordance with CO adsorption on single crystal ZnO(10 $\bar{1}$ 0)

and could be assigned to CO adsorbed on Zn²⁺ cations,⁴⁸ suggesting that adsorption sites on powder ZnO catalysts are equivalent to the sites on ZnO(10 $\bar{1}$ 0). In comparison, CO adsorption on reduced ZnO at 120 K [Fig. 3(a)] showed the same CO peak with no difference in peak position or intensity, when compared to the IR spectra of CO adsorption on oxidized ZnO. This is rather surprising since CO has been employed to detect surface defects of reducible metal oxides, such as TiO₂ and CeO₂.^{7,8} As a comparison, CO adsorption on CeO₂ nanorods was also performed [Fig. 3(b)]. On oxidized CeO₂ nanorods, which was annealed in 0.1 mbar O₂ at 473 K, two sharp peaks at 2173 cm⁻¹ and 2154 cm⁻¹ were observed. After CeO₂ nanorods were reduced with 10 mbar H₂, the 2173 cm⁻¹ peak shifts to 2171 cm⁻¹, which was accompanied by an obvious increase in peak intensity. Accordingly, the 2154 cm⁻¹ peak has been assigned to CO on Ce⁴⁺ cations, while the 2173 cm⁻¹ peak was assigned to CO on Ce³⁺ cations in previous studies.^{7,10} The residual 2173 cm⁻¹ peak on oxidized CeO₂ nanorods is likely due to CO adsorption at the steps and kinks of CeO₂ nanorods. Nevertheless, our IR spectroscopy results showed that Ce³⁺-related CO peaks grew drastically on reduced CeO₂, demonstrating the feasibility of using CO to titrate surface defects of CeO₂.

To understand the mechanism underlying the different adsorption behavior of CO on ZnO, CO adsorption on different Zn_{3c} sites of stoichiometric and reduced ZnO(10 $\bar{1}$ 0) surfaces was calculated accordingly, as shown in Figs. 4(a) and 4(b). Figure 4(c) showed that although the calculated frequency of CO on site 1 (2092 cm⁻¹) is largely red-shifted from those on sites 2–4 (2145–2148 cm⁻¹), the binding energy of CO on site 1 and site 3 is only 0.23 eV and 0.24 eV, respectively, which is lower than those on sites 2 and 4 (0.34 eV and 0.37 eV). Therefore, the adsorption of CO on Zn_{3c} sites around oxygen vacancies (Vo) is prohibited, leading to its insensitivity in identifying surface oxygen vacancies of ZnO.

Thus, a probe molecule with a strong adsorbate–Vo interaction is required. We chose formaldehyde (CH₂O) because of its structural simplicity and similar configuration to CO. Figure 3(c) displayed the

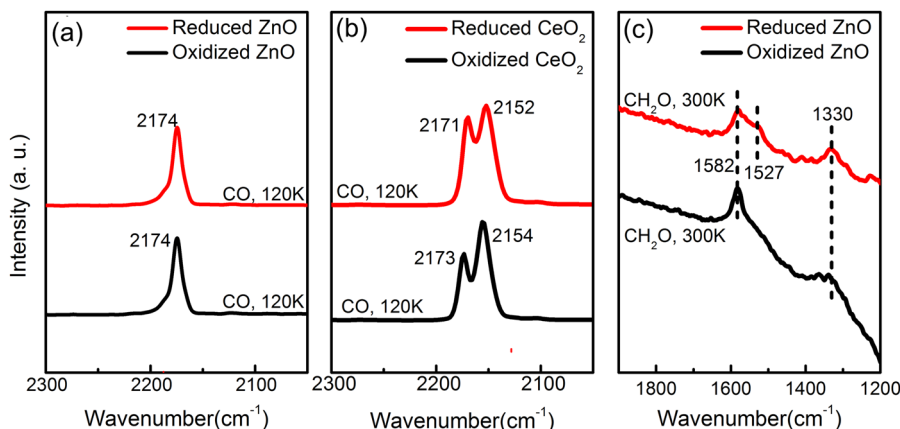


FIG. 3. (a) Transmission IR spectra of ZnO powder exposed to 0.001 mbar CO at 120 K; (b) transmission IR spectra of CeO₂ nanorods exposed to 0.001 mbar CO at 120 K; and (c) transmission IR spectra of ZnO powder exposed to 0.001 mbar CH₂O at 300 K. The oxidized ZnO and CeO₂ samples were prepared by annealing in 0.1 mbar O₂ at 673 K and 473 K, respectively. The reduced ZnO powders were prepared by annealing in 10 mbar CO at 673 K, and the CeO₂ nanorods were prepared by annealing in 10 mbar H₂ at 533 K. Lower thermal treatment temperature was used for CeO₂ than ZnO, in order to maintain their morphology. IR spectra in (a) and (b) were recorded at 120 K, while spectra in (c) was recorded at 300 K.

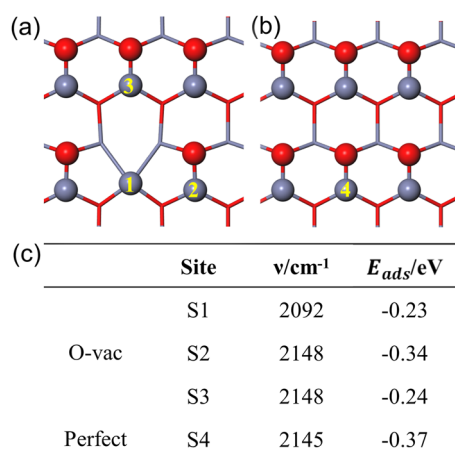


FIG. 4. The configurations of CO adsorption on (a) Zn_{3c} sites around Vo and (b) regular Zn_{3c} site, and (c) their corresponding calculated vibrational frequencies and binding energies.

IR spectra of CH_2O adsorption on oxidized ZnO surfaces at room temperature, exhibiting two peaks at 1582 cm^{-1} and 1330 cm^{-1} , respectively. Note that these bands are totally different from molecularly adsorbed CH_2O , which shows a single peak of $\text{C}=\text{O}$ vibration at 1700 cm^{-1} , close to that of gas phase CH_2O .⁴⁹ Instead, the formate species on ZnO are known to exhibit two peaks at 1575 cm^{-1} and 1367 cm^{-1} ,⁵⁰ close to the positions of the pair of peaks observed above. For CH_2O adsorption on reduced ZnO [Fig. 3(c)], an additional peak at 1527 cm^{-1} was also observed besides the pair of peaks observed on oxidized ZnO. We thus speculated that the 1527 cm^{-1} peak that originates from CH_2O are adsorbed at Vo sites. The redshift of frequency with respect to gas phase CH_2O can be rationalized by the weakened $\text{C}=\text{O}$ stretching vibration that arose from the strong $\text{CH}_2\text{O}-\text{Vo}$ interaction.

CH_2O adsorption on single crystal $\text{ZnO}(10\bar{1}0)$ surfaces was also investigated by SRPES. Figure 5(a) showed that, after the exposure of 3 L CH_2O to the $\text{ZnO}(10\bar{1}0)$ surface at 120 K, the C 1s peak appeared first at 289.1 eV and shifted gradually to 290.2 eV with increasing temperatures. Previous studies^{29,51} have attributed the 289.1 eV peak to molecularly adsorbed CH_2O on ZnO, while the 290.2 eV peak is assigned to $\text{O}-\text{C}-\text{O}$ species, e.g., formate. Consistently, the adsorption of CH_2O at room temperature gave rise to a C 1s peak at 290.2 eV directly [Fig. 5(b)]. Combined with the observed IR vibrational features at 1582 cm^{-1} and 1330 cm^{-1} in Fig. 3(c), we thus concluded that CH_2O has reacted with ZnO to form formate at 300 K. Meanwhile, for CH_2O on stoichiometric ZnO surfaces [Fig. 5(b)], the weak peak at 287.7 eV could be assigned to the small amount of molecularly adsorbed CH_2O (denoted as $\text{CH}_2\text{O}/\text{ZnO}$). Furthermore, CH_2O adsorption on Zn/ZnO($10\bar{1}0$) surfaces with various Zn coverage was also studied by SRPES. On the 0.6 ML ZnO/ZnO($10\bar{1}0$) surface, the intensity of formate was found to increase [Fig. 5(b)], which could be attributed to the roughening of the ZnO surface, caused by the formation of reduced ZnO clusters from Zn deposition on ZnO. Upon deposition, metallic Zn reacted with lattice oxygen of ZnO and led to the formation of ZnO clusters, which increased the total surface

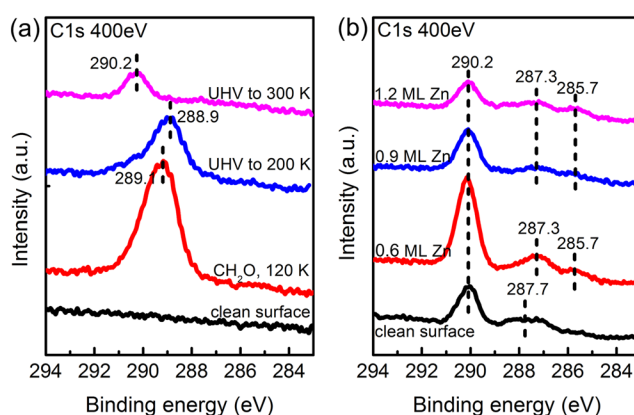


FIG. 5. (a) C 1s spectra of CH_2O adsorption (3 L) at 120 K on the $\text{ZnO}(10\bar{1}0)$ surface, which was then annealed to 200 K, 300 K, and 450 K, respectively. All C 1s spectra were recorded at 120 K. (b) C 1s spectra of CH_2O adsorption (3 L) at 300 K on a single crystal $\text{ZnO}(10\bar{1}0)$ surface deposited with a different coverage of metallic Zn, respectively.

area and caused the increase in the surface formate peak. A new C 1s peak at 287.3 eV could be attributed to CH_2O adsorbed at surface defect sites or more specifically at Vo sites (denoted as $\text{CH}_2\text{O}/\text{Vo}$). Additionally, a weak C 1s peak at 285.7 eV could be assigned as the CH_2O peak on the more-reduced or metallic Zn sites (denoted as $\text{CH}_2\text{O}/\text{Zn}$). Consistently, for the adsorption of CH_2O on Zn/ZnO($10\bar{1}0$) surfaces, both C 1s peaks of formate and $\text{CH}_2\text{O}/\text{Vo}$ decrease with the increasing Zn coverage (0.9 ML and 1.2 ML), owing to the coverage of the ZnO surface by metallic Zn atoms.

DFT calculations were performed to identify the adsorption and dehydrogenation of CH_2O on stoichiometric and reduced ZnO, respectively. In Fig. 6(a), CH_2O adsorbs on the Zn_{3c} site of the stoichiometric $\text{ZnO}(10\bar{1}0)$ surface via end O atoms, with the calculated adsorption energy of 0.49 eV apparently higher than CO adsorption. The calculated frequency of CH_2O is 1692 cm^{-1} of $\text{C}=\text{O}$, close to that of gas phase CH_2O . By crossing a barrier of 1.17 eV, CH_2O can dehydrogenate to form CHO^* species and transfer one proton to the adjacent surface oxygen site, as shown in Fig. 6(b). Afterward, the CHO^* species relaxed to formate of tridentate configuration, with a barrier of 0.75 eV. The lateral proton diffuses away due to the repulsive interaction from adjacent formate, with an exothermic energy of 0.74 eV. The corresponding calculated frequencies of formate are 1568 cm^{-1} and 1331 cm^{-1} , well in accordance with the experimentally observed IR peaks of formate at 1582 cm^{-1} and 1330 cm^{-1} in Fig. 3(c).

Figure 6(c) displays the dehydrogenation process of CH_2O on the reduced $\text{ZnO}(10\bar{1}0)$ surface. Assuming that ZnO underwent a substantial reduction by CO, we used a structural model removing a row of oxygen atoms along the $[1\bar{2}10]$ direction on $\text{ZnO}(10\bar{1}0)$. CH_2O adsorbs at the surface Zn site adjacent to Vo rows with the adsorption energy of 0.25 eV. Then, with crossing an activation barrier of 0.45 eV, the adsorbed CH_2O relaxed to CHO^* species at exposed Vo rows. The formed CHO^* binds at the bridging Zn-Zn site, exhibiting a vibration signal of $\text{C}=\text{O}$ at 1520 cm^{-1} , well consistent with the experimentally observed 1527 cm^{-1} peaks for

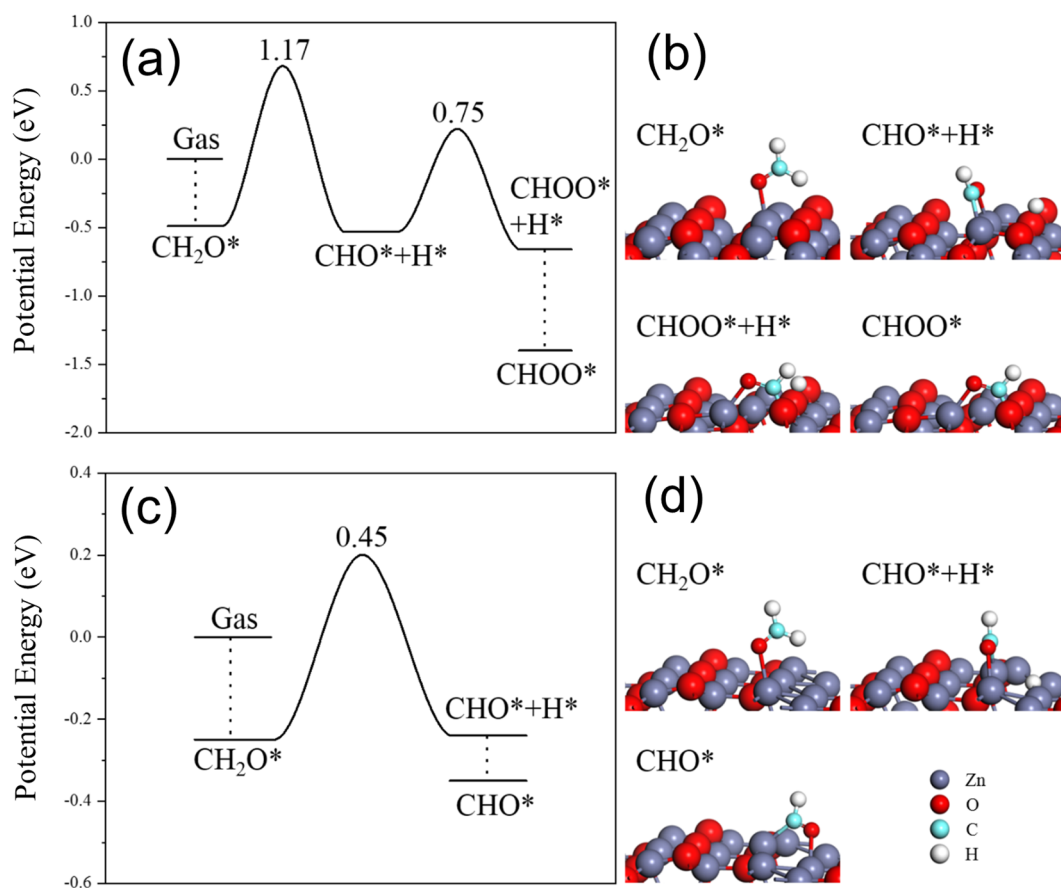


FIG. 6. (a) The potential energy surface and (b) intermediate configuration of CH₂O dehydrogenation on the stoichiometric ZnO(10 $\bar{1}$ 0) surface; (c) the potential energy surface and (d) intermediate configuration of CH₂O dehydrogenation on the reduced ZnO(10 $\bar{1}$ 0) surface. * represents adsorbed species.

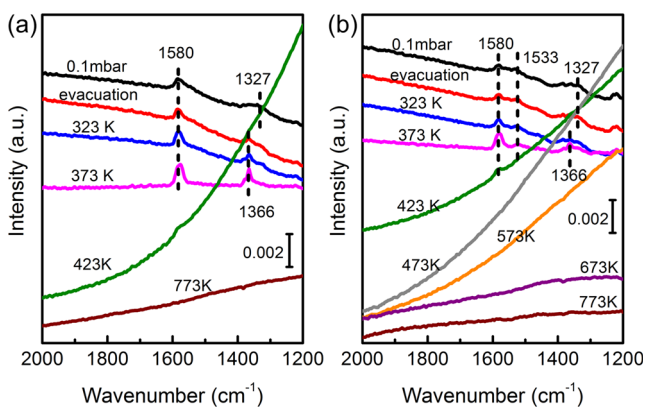


FIG. 7. Transmission IR spectra of ZnO powder exposed to 0.1 mbar CH₂O at 300 K and then evacuated and annealed to 373 K, 423 K, 473 K, 573 K, 673 K, and 773 K subsequently. (a) Oxidized ZnO surfaces and (b) reduced ZnO surfaces. All spectra were recorded at 300 K.

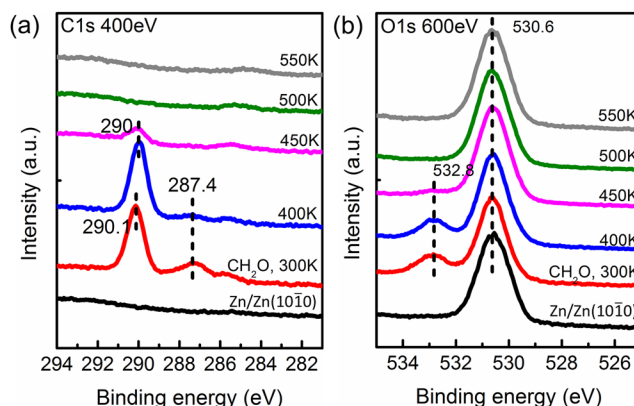


FIG. 8. (a) C 1s spectra and (b) O 1s spectra of CH₂O adsorption (3 L) on the 0.6 ML Zn/ZnO(10 $\bar{1}$ 0) surface at 300 K, which was annealed to 400 K, 450 K, 500 K, and 550 K subsequently.

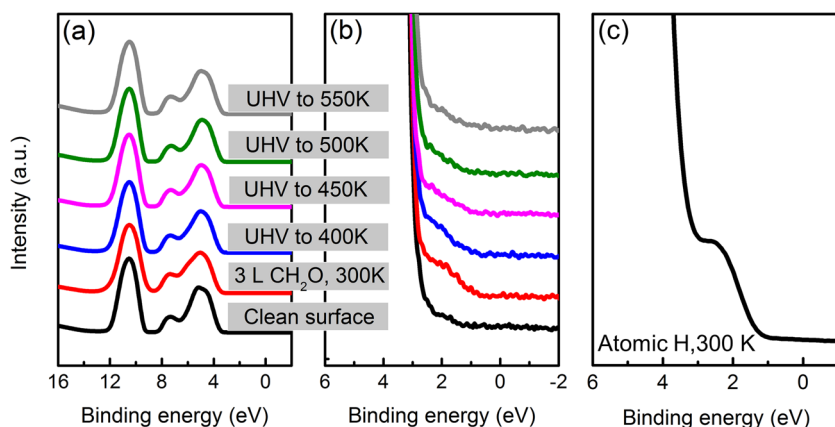


FIG. 9. [(a) and (b)] Valence band spectra of CH₂O adsorption (3 L) on a clean ZnO(10 $\bar{1}$ 0) surface at 300 K, which was annealed to 400 K, 450 K, 500 K, and 550 K subsequently. The spectra in (a) near the Fermi level is magnified in (b). (c) Valence band spectra of a ZnO(10 $\bar{1}$ 0) surface after the exposure to 15 L atomic H at 300 K. Exposure to atomic hydrogen was performed by dissociating H₂ on a hot tungsten filament situated in the line of sight from the substrate.

CH₂O adsorption on reduced ZnO. Trapped at Vo sites with the lack of surrounding surface oxygen, the formed CHO* cannot transform into formate species.

Using CH₂O as a probe molecule, we could detect surface defects of ZnO using both IR spectroscopy and SRPES, which is vital to clarify the chemical nature of surface active sites on ZnO-based catalysts for reactions such as methanol synthesis, water shift reaction, and syngas-to-olefin reactions.

C. CH₂O dehydrogenation on ZnO surfaces

Figure 7 compared IR spectra for CH₂O adsorption on oxidized and reduced ZnO surfaces, respectively. On the oxidized ZnO surface [Fig. 7(a)], the annealing of adsorbed CH₂O to 373 K led to increased peak intensity of formate with sharper line shapes, while the frequency of $\nu_s(\text{OCO})$ peak shifts from 1327 cm⁻¹ to 1366 cm⁻¹, indicating the occurrence of relaxation and ordering of formate geometry at 373 K. Further annealing to 423 K led to the disappearance of formate features, and the baseline at a low wavenumber region shifts to a higher position. The spectra shift indicates an increase in the absorption of IR light, which has been used to study the hydrogen doping effect in ZnO bulk by ascribing it to the IR absorption of free charge carriers.^{52–54} Accordingly, the baseline shift in Fig. 7(a) demonstrates that the CH₂O dehydrogenation reaction occurs on the ZnO surface at 423 K. At the same time, the generated hydrogen atoms diffuse into the bulk, forming H interstitials in the subsurface region. The temperature of 423 K is in accordance with the reported activation barrier of 1 eV for H atom diffusion in bulk ZnO.⁵⁵ Further annealing to higher temperatures caused the reduction of baseline gradually, which became flat again after the annealing at 773 K, indicating the migration of H interstitials back to the surface and their desorption at high temperature. Similarly, annealing the reduced ZnO surface covered with CH₂O [Fig. 7(b)] found the direct desorption of CH₂O species at Vo sites at 423 K. The subsequent dehydrogenation reaction is approximately the same as that on oxidized surfaces, suggesting that surface Zn_{3c} sites rather than Vo sites are active centers for CH₂O dehydrogenation.

CH₂O dehydrogenation on ZnO(10 $\bar{1}$ 0) surfaces was examined by SRPES. From both C 1s and O 1s spectra (Fig. 8), CH₂O adsorbed

at Vo sites (287.4 eV) desorbs first at 400 K, followed by the desorption of formate species at 450 K, consistent with IR spectroscopy results of CH₂O decomposition on ZnO. To further obtain the information on atomic H, the corresponding characterization of valence band spectra was also performed. As shown in Figs. 9(a) and 9(b), once the ZnO surface was exposed to CH₂O at 300 K, an obvious shoulder appears at 1 eV above the valence band maximum (VBM). Subsequently, the shoulder gap state gradually decreases and almost disappears at 450 K. A similar band gap state can be observed after exposing atomic H to ZnO surfaces in Fig. 9(c), which can be regarded as a characteristic of H donor states. Note that the temperature for the disappearance of the H donor state just corresponds to the maximum of the baseline shift in Fig. 7, which could be attributed to the different detection depth between soft X-ray (1–3 nm) and infrared light (200 nm). We speculated that CH₂O dehydrogenates first to form formate at 300 K, accompanying the appearance of the surface H donor state in valence band spectra. The subsequent dehydrogenation process at 450 K led to the incorporation of subsurface interstitial H atoms, resulting in a large shift in the baseline of IR spectra. The residual decomposition products are likely to desorb at 450 K, which consist mainly of CO and CO₂ based on recent TPD studies.⁵⁶

IV. CONCLUSIONS

Surface defect sites from bare ZnO surfaces are found difficult to probe by SRPES and IR spectroscopy, either directly or using CO as a probe molecule. Instead, we found that formaldehyde is a suitable molecule to titrate surface oxygen vacancies, both for SRPES characterization over ZnO(10 $\bar{1}$ 0) and transmission infrared (IR) spectroscopy over powder ZnO. DFT calculations revealed that formaldehyde dissociates on the ZnO surface to form formate and formyl on the stoichiometric surface and the reduced surface, respectively. Furthermore, the mechanism of formaldehyde dehydrogenation on ZnO surfaces was also elucidated, while the generated hydrogen atoms are found to be stored in ZnO bulk from 423 K to 773 K, which shows potential in the hydrogenation reaction over ZnO catalysts.

AUTHOR'S CONTRIBUTIONS

Y. Cao and J. Luo contributed equally to this work.

ACKNOWLEDGMENTS

This work was financially supported by the Ministry of Science and Technology of China (Grant Nos. 2017YFB0602205 and 2016YFA0202803), the Strategic Priority Research Program of the Chinese Academy of Sciences (Grant No. XDB17020200), and the Natural Science Foundation of China (Grant Nos. 21972144, 21473191, 91545204, and 91645202). We thank Na Li and Beibei Wang for providing the powder catalysts.

REFERENCES

- S. T. Bromley, P. Moreira Ide, K. M. Neyman, and F. Illas, *Chem. Soc. Rev.* **38**, 2657 (2009).
- F. De Angelis, C. Di Valentin, S. Fantacci, A. Vittadini, and A. Selloni, *Chem. Rev.* **114**, 9708 (2014).
- S. Chen, F. Xiong, and W. Huang, *Surf. Sci. Rep.* **74**, 100471 (2019).
- D. W. Goodman, *Chem. Rev.* **95**, 523 (1995).
- L. Fiermans, R. Hoogewijs, and J. Vennik, *Surf. Sci.* **47**, 1 (1975).
- L. Nguyen, F. F. Tao, Y. Tang, J. Dou, and X. J. Bao, *Chem. Rev.* **119**, 6822 (2019).
- C. W. Yang, L. L. Yin, F. Bebensee, M. Buchholz, H. Sezen, S. Heissler, J. Chen, A. Nefedov, H. Idriss, X. Q. Gong, and C. Woll, *Phys. Chem. Chem. Phys.* **16**, 24165 (2014).
- M. Xu, H. Noei, K. Fink, M. Muhler, Y. Wang, and C. Woll, *Angew. Chem., Int. Ed.* **51**, 4731 (2012).
- C. Yang, X. Yu, S. Heissler, A. Nefedov, S. Colussi, J. Llorca, A. Trovarelli, Y. Wang, and C. Woll, *Angew. Chem., Int. Ed.* **56**, 375 (2017).
- A. Chen, X. Yu, Y. Zhou, S. Miao, Y. Li, S. Kuld, J. Sehested, J. Liu, T. Aoki, S. Hong, M. F. Camellone, S. Fabris, J. Ning, C. Jin, C. Yang, A. Nefedov, C. Wöll, Y. Wang, and W. Shen, *Nat. Catal.* **2**, 334 (2019).
- N. Nilius and H. J. Freund, *Acc. Chem. Res.* **48**, 1532 (2015).
- S. Kattel, P. J. Ramirez, J. G. Chen, J. A. Rodriguez, and P. Liu, *Science* **355**, 1296 (2017).
- S. Kuld, M. Thorhauge, H. Falsig, C. F. Elkjaer, S. Helveg, I. Chorkendorff, and J. Sehested, *Science* **352**, 969 (2016).
- M. Behrens, F. Studt, I. Kasatkin, S. Kuhl, M. Havecker, F. Abild-Pedersen, S. Zander, F. Girgsdies, P. Kurr, B. L. Knief, M. Tovar, R. W. Fischer, J. K. Nørskov, and R. Schlögl, *Science* **336**, 893 (2012).
- F. Jiao, J. Li, X. Pan, J. Xiao, H. Li, H. Ma, M. Wei, Y. Pan, Z. Zhou, M. Li, S. Miao, J. Li, Y. Zhu, D. Xiao, T. He, J. Yang, F. Qi, Q. Fu, and X. Bao, *Science* **351**, 1065 (2016).
- J. A. Rodriguez, P. Liu, J. Hrbek, J. Evans, and M. Pérez, *Angew. Chem., Int. Ed.* **46**, 1329 (2007).
- C. Rhodes, G. J. Hutchings, and A. M. Ward, *Catal. Today* **23**, 43 (1995).
- W. Jin, G. Chen, X. Duan, Y. Yin, H. Ye, D. Wang, J. Yu, X. Mei, and Y. Wu, *Appl. Surf. Sci.* **423**, 451 (2017).
- C. Wu, *Appl. Surf. Sci.* **319**, 237 (2014).
- L. Zhang, J. Zhao, J. Zheng, L. Li, and Z. Zhu, *Appl. Surf. Sci.* **258**, 711 (2011).
- N. Li, F. Jiao, X. Pan, Y. Ding, J. Feng, and X. Bao, *ACS Catal.* **9**, 960 (2019).
- X. Liu, K. Zhou, L. Wang, B. Wang, and Y. Li, *J. Am. Chem. Soc.* **131**, 3140–3141 (2009).
- G. Kresse and J. Furthmüller, *Comp. Mater. Sci.* **6**, 15 (1996).
- G. Kresse and J. Furthmüller, *Phys. Rev. B* **54**, 11169 (1996).
- P. E. Blöchl, *Phys. Rev. B* **50**, 17953 (1994).
- G. Kresse and D. Joubert, *Phys. Rev. B* **59**, 1758 (1999).
- J. P. Perdew, K. Burke, and M. Ernzerhof, *Phys. Rev. Lett.* **77**, 3865 (1996).
- X.-K. Gu, C.-Q. Huang, and W.-X. Li, *Catal. Sci. Technol.* **7**, 4294 (2017).
- R. Pala and H. Metiu, *J. Catal.* **254**, 325 (2008).
- B. Meyer, H. Rabaa, and D. Marx, *Phys. Chem. Chem. Phys.* **8**, 1513 (2006).
- J. Tersoff and D. R. Hamann, *Phys. Rev. Lett.* **50**, 1998 (1983).
- J. Tersoff and D. R. Hamann, *Phys. Rev. B* **31**, 805 (1985).
- W. A. Hofer, *Prog. Surf. Sci.* **71**, 147 (2003).
- R. Kovacic, B. Meyer, and D. Marx, *Angew. Chem., Int. Ed.* **46**, 4894 (2007).
- P. Schroer, P. Kruger, and J. Pollmann, *Phys. Rev. B* **49**, 17092 (1994).
- X. L. Yin, A. Birkner, K. Hanel, T. Lober, U. Kohler, and C. Woll, *Phys. Chem. Chem. Phys.* **8**, 1477 (2006).
- X. Shao, K.-i. Fukui, H. Kondoh, M. Shionoya, and Y. Iwasawa, *J. Phys. Chem. C* **113**, 14356 (2009).
- C. Wöll, *Prog. Surf. Sci.* **82**, 55 (2007).
- J. Nakamura, *Top. Catal.* **22**, 277 (2003).
- M. F. Guimon, G. Pfister-Guillouzo, M. Bremont, W. Brockmann, C. Quet, and J. Y. Chenard, *Appl. Surf. Sci.* **108**, 149 (1997).
- T. Fujitani, I. Nakamura, T. Uchijima, and J. Nakamura, *Surf. Sci.* **383**, 285 (1997).
- M. C. Biesinger, L. W. M. Lau, A. R. Gerson, and R. S. C. Smart, *Appl. Surf. Sci.* **257**, 887 (2010).
- Y. Wang and C. Woll, *Chem. Soc. Rev.* **46**, 1875 (2017).
- M. Xu, Y. Gao, E. M. Moreno, M. Kunst, M. Muhler, Y. Wang, H. Idriss, and C. Wöll, *Phys. Rev. Lett.* **106**, 138302 (2011).
- Y. Wang, A. Glenz, M. Muhler, and C. Woll, *Rev. Sci. Instrum.* **80**, 113108 (2009).
- D. Scarano, G. Spoto, S. Bordiga, A. Zecchina, and C. Lamberti, *Surf. Sci.* **276**, 281 (1992).
- Z. Geng, X. Kong, W. Chen, H. Su, Y. Liu, F. Cai, G. Wang, and J. Zeng, *Angew. Chem., Int. Ed.* **57**, 6054 (2018).
- M. Buchholz, X. J. Yu, C. W. Yang, S. Heissler, A. Nefedov, Y. M. Wang, and C. Woll, *Surf. Sci.* **652**, 247 (2016).
- X. Yu, Z. Zhang, C. Yang, F. Bebensee, S. Heissler, A. Nefedov, M. Tang, Q. Ge, L. Chen, B. D. Kay, Z. Dohnálek, Y. Wang, and C. Wöll, *J. Phys. Chem. C* **120**, 12626 (2016).
- G. Hussain and N. Sheppard, *Spectrochim. Acta, Part A* **43**, 1631 (1987).
- Z. Wang, F. Xiong, Z. Zhang, G. Sun, H. Xu, P. Chai, and W. Huang, *J. Phys. Chem. C* **121**, 25921 (2017).
- D. A. Panayotov and J. T. Yates, *Chem. Phys. Lett.* **436**, 204 (2007).
- H. Noei, H. Qiu, Y. Wang, M. Muhler, and C. Woll, *ChemPhysChem* **11**, 3604 (2010).
- X. Wang, B. Lu, L. Li, and H. Qiu, *ChemistryOpen* **7**, 491 (2018).
- H. Qiu, B. Meyer, Y. Wang, and C. Woll, *Phys. Rev. Lett.* **101**, 236401 (2008).
- L. Li, Y. Du, X. Wang, J. Han, and C. Wang, *Imaging Sci. Photochem.* **36**, 171 (2018).